

# Combined Receiver-Function and Surface Wave Phase-Velocity Inversion Using a Niching Genetic Algorithm: Application to Patagonia

by Jesse F. Lawrence and Douglas A. Wiens

**Abstract** A combined inversion of body wave receiver functions and Rayleigh wave phase velocities using a niching genetic algorithm (NGA) increases the uniqueness of the solution over separate inversions and also facilitates explicit parameterization of layer thickness in the model space. This parameterization requires fewer layers and *a priori* constraints for modeling more complex structures than traditional linearized inversion. NGAs solve for a suite of locally optimal solutions in addition to isolating the globally optimal solution by using an evolutionary paradigm. This nonlinear examination of the error space provides an opportunity to examine trade-off within the model space. The method, when applied to synthetic data, locates interfaces within 2 km of the test structure and identifies appropriate structure and velocity. Applying this method to data from a deployment of five broadband stations in Chilean Patagonia yields a regional model of crustal structure that is consistent with the geological history of the region. Sediment thickness is inversely proportional to crustal thickness, with sediment thicknesses reaching more than 4 km, where the crustal thickness thins to 28 km. This is consistent with previous geological studies, which suggests that the Rocas Verdes basin in western Patagonia formed by crustal thinning, isostatic compensation, and subsequent sedimentation.

## Introduction

Surface wave phase-velocity dispersion and *P*-wave receiver-function inversion techniques provide complementary information regarding crustal and upper mantle structure. Previous studies show that receiver-function methods are efficient tools for determining Moho depth (Sheehan, 1995), crustal velocity models (Cassidy, 1995; Owens *et al.*, 1984), depths to upper mantle discontinuities (Dueker and Sheehan, 1997), and even isolation of low-velocity layers (Cassidy, 1995). However, receiver functions are mostly sensitive to sharp velocity contrasts and relatively insensitive to the average velocity and smooth velocity gradients. Phase-velocity dispersion analysis is a time-tested tool that is sensitive to average shear velocity over a broad range of depths between two seismic stations. Although extremely useful for determining the general velocity profile with depth, dispersion techniques are largely insensitive to velocity discontinuities. Combining these complimentary tools in a single inversion allows for more unique analyses of crustal and upper mantle structure (Julia *et al.*, 2000).

Several different groups have previously combined analyses of receiver functions and surface wave phase velocities. Last *et al.* (1997) suggest that forward modeling receiver functions and surface wave dispersion measurements can result in more unique solutions than either of the techniques in isolation. Augmentations of the linearized

receiver-function inversion to account for dispersion greatly reduce the linearized inversion's dependence on starting models (Ozalaybey *et al.*, 1997; Du and Foulger, 1999; Julia *et al.*, 2000). However, each of these techniques requires starting models based on *a priori* knowledge. Genetic algorithms (Clitheroe *et al.*, 2000; Shibusaki *et al.*, 1996), neighborhood algorithms (Sambridge, 1999a,b), and the niching genetic algorithm (NGA) reduce the need for *a priori* constraints when applied to the combined receiver-function and phase-velocity problem.

In this study we use a NGA, which uses an evolutionary paradigm, to isolate the globally optimal model and several locally optimal modes for reproducing observed receiver functions and phase velocity-dispersion curves. By comparing dispersion-curve and receiver-function misfit cost simultaneously and separately, we can attribute resultant model characteristics to particular data variations. The NGA also allows simultaneous determination of layer thickness and velocity without *a priori* constraints, which is otherwise difficult with linearized inversion techniques.

We demonstrate the usefulness of applying a NGA to the combined phase-velocity dispersion and receiver-function problem. The NGA isolates geologically reasonable 1D seismic profiles that account for both surface wave dispersion curves and receiver functions without requiring significant

*a priori* constraints. In this article we present the assumptions, limitations, and advances made by the NGA combined phase-velocity and receiver-function algorithm. First, we describe the search algorithm, the receiver-function technique, and the surface wave dispersion techniques used here. Then we demonstrate the procedure by using synthetic data. Finally, we use the technique to invert broadband data collected by a regional deployment in Chilean Patagonia (Wiens, 1998).

## Methodology

### Niching Genetic Algorithms

The NGA (Mafoud, 1995) is a compound form of genetic algorithm (GA) that searches a given model space for optimal solutions to an objective function. For a more comprehensive discussion of GAs and NGAs, refer to Goldberg (1989) and Koper *et al.* (1999). Typical genetic algorithms operate by randomly creating a population of models and evaluating the misfit cost between the model and an objective cost function (in this case, the misfit with the observed data). The GA then produces a new generation of models by combining the characteristics of the previous generation in a way that simulates genetic reproduction. The success of a given model in transmitting its characteristics into the next generation is controlled by the misfit cost. In this manner, after several generations, much of the model space may be searched, leaving only optimal models.

The NGA deviates from the traditional GA by allowing multiple subpopulations, called “demes,” to search the model space. A cost associated with similarity between models of different demes is added to the objective function to ensure that each deme searches a different region in the model space. This allows the method to locate several locally optimal models and the globally optimal model. Comparison between various optimal solutions facilitates analysis of parameter trade-offs within the system.

The NGA only requires a defined model space, a specified number of generations, a number of models, and a number of demes. There is no dependence on a starting model because the first-generation models are randomly generated. Experiments with repeated inversions using multiple randomizing kernels suggest that each inversion searches the full model space with sufficient randomization. Additionally, models in separate demes are required to be dissimilar, meaning that models are discouraged from prematurely converging on a single model type.

### Receiver Functions

Receiver functions represent the local earth response to the arrival of nearly vertical *P* waves beneath a three-component broadband seismometer. At any subhorizontal interface with sufficient impedance contrasts, a portion of the subvertical *P*-wave energy converts to a *Ps* phase (Fig. 1). Mathematically, the receiver function is the transfer

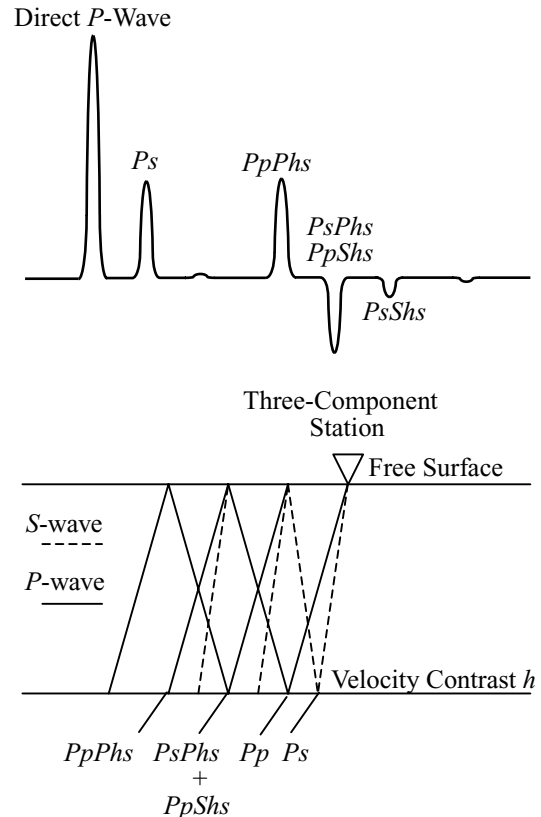


Figure 1. A graphical representation of receiver functions.

function between the *P* wave with all associated *P* multiples and reverberations and the *Ps* phases with their multiples and reverberations (Ammon, 1991). Radial component seismograms record *P*-to-*S* conversions and multiple reverberations shortly after the initial *P* waves (Burdick and Langston, 1977). Receiver functions may be mathematically estimated as the transfer functions between radial and vertical time series.

We choose the forward modeling technique of Randall (1989) to produce synthetic receiver functions for use with NGA-simulated inversion. The forward modeling algorithm is computationally inexpensive and works well for all regions with horizontal to subhorizontal layer geometry. The numerical calculation produces radial and vertical synthetic local earth responses to an incident *P* wave, assuming plane-wave ground motions using the reflectivity method of Kennett (1983). The vertical earth response is deconvolved from the radial to produce the synthetic receiver function (Langston, 1979).

Several techniques exist for estimating receiver functions from observed data (e.g., Clayton and Wiggins, 1976; Park and Levin, 2000; Gurrrola *et al.*, 1995). We use the iterative deconvolution technique (Ligorria and Ammon, 1999) to approximate receiver functions from observed data for two main reasons. First, the iterative method creates a causal receiver function. Second, iterative deconvolution

provides quantitative estimates of receiver function reliability, making stacking more reliable. Receiver functions produced with spectral division are also compared with the iterative deconvolution receiver functions as a secondary check. More comprehensive discussions may be found in Ammon (1991) and Ligorría and Ammon (1999).

One of the major hindrances to receiver-function analysis is its nonunique nature (Ammon *et al.*, 1990). The receiver function's amplitude depends on impedance contrast. The arrival time of any phase depends on both the velocity and the depth of impedance contrasts, which results in large trade-offs between the two. Traditionally, receiver-function studies treat the inversion as a linearized inversion. The application of a linear inversion process to a nonlinear inverse problem often causes bias and nonuniqueness (Menke, 1984). Recent efforts using linearized inversions of both receiver functions and group velocity curves have reduced nonuniqueness (Julia *et al.*, 2000). However, linearized inversion techniques can only invert for  $S$ -wave velocity when given *a priori* constraints on layer thickness, density, and  $V_P/V_S$  ratios. The solution-to-layer velocity cannot be uniquely solved for without also solving for layer thickness simultaneously. The NGA requires neither *a priori* constraints.

#### Surface Wave Phase Velocities

Phase-velocity dispersion primarily depends on  $S$  velocity with some dependence on  $P$  velocity and little dependence on density (Aki and Richards, 1980; Takeuchi and Saito, 1972). The sensitivity of the fundamental mode to velocity at depth varies with period. We choose to use interstation Love and Rayleigh phase-velocity dispersion in combination with receiver function analysis for several reasons. First, the forward model of dispersion is a relatively efficient numerical computation (Herrmann, 1978). Second, interstation phase velocity can be measured on small lateral scales in dense seismic arrays. Third, inverting both Love and Rayleigh wave phase-velocity dispersion simultaneously for structure should provide greater depth constraints on velocities, because each is sensitive to different depth ranges. Finally, surface wave dispersion has been shown to improve inversions of receiver functions for crustal structure (Ozalaybey *et al.*, 1997; Du and Foulger, 1999; Julia *et al.*, 2000).

We measure interstation Love and Rayleigh phase velocity by first "cleaning" the surface wave with the phase-matched filter technique (Herrin and Goforth, 1977) and then applying the modal isolation technique similar to Hwang and Mitchell (1986). Finally we determine phase delay by using cross correlation between narrow bandpass-filtered auto and cross correlelograms. The combination of these two techniques increases the signal-to-noise ratio by isolating the fundamental mode before determining phase velocity. Phase velocities are determined for all events having a backazimuth within  $5^\circ$  of the interstation azimuth. Phase velocities for each period are averaged for each station so that the

measured dispersion is more representative of the structure underlying that station. We preferentially sample shorter period measurements to increase the importance of shallow layers ( $<55$  km), but we continue sampling to periods of 120 sec. To increase resolution and importance of shallow structure we require the modeled phase-velocity curve to match a greater number of discrete shorter-period phase velocities than longer-period phase velocities. We also use about 40% more Rayleigh velocities than Love velocities to place greater emphasis on Rayleigh wave dispersion, because Rayleigh mode isolation is less difficult.

#### The Inverse Problem

We invert for a nine-layer model of seismic structure with a NGA with 20 models per deme, four demes per generation, and 250 generations. The parameterization of a model is an *a priori* constraint that is unavoidable for any modeling process. Therefore, we endeavor to minimize bias because of our parameterization. The NGA systematically creates 20,000 models with nine independent shear velocities ( $V_S$ ), eight independent layer thicknesses ( $H$ ) overlying a half-space, and five independent  $P$ -to- $S$  velocity ratios ( $V_P/V_S$ ), within the model space described in Table 1. For each model we calculate an objective cost from the second derivative roughness estimate, the standard deviation between the forward modeled receiver function and the observed receiver function, and the standard deviation between the forward modeled dispersion curves and the observed dispersion curves for both Love and Rayleigh waves. The objective cost function may be expressed as,

$$\text{Cost} = \left[ \sum_{i=1}^9 (V_{S_i} - 2V_{S_{i+1}} + V_{S_{i+2}}) \right]^{RW} \left[ \sqrt{\sum_{j=1}^N (R_{\text{obs}_j} - R_{\text{syn}_j})^2 W_j / N} \right] \left[ \sqrt{\sum_{k=1}^M (D_{\text{obs}_j} - D_{\text{syn}_j}) / M} \right]^{SW},$$

where  $V_S$  is the shear velocity,  $RW$  is the roughness weight-

Table 1  
Model Parameterization

Layer	$H$		$V_S$		$V_P/V_S$	
	Min	Max	Min	Max	Min	Max
1	0.25	10	1.70	3.75		
2	0.25	10	1.70	3.75	1.69	1.78
3	0.25	10	2.20	4.20		
4	0.25	10	2.20	4.80	1.69	1.78
5	0.25	10	2.20	4.80		
6	0.25	10	3.00	4.80	1.69	1.78
7	0.25	10	3.75	4.80		
8	0.25	10	4.20	4.80	1.69	1.78
9	Half-space		4.40	4.80	1.69	1.78

The ranges of the 22 independent parameters in a nine-layer NGA problem are shown. There are eight thickness parameters, nine  $V_S$  parameters, and five  $V_P/V_S$  parameters. Min, minimum; Max, maximum.

ing,  $R_{\text{obs}}$  and  $R_{\text{syn}}$  are the observed and synthetic receiver-function values with  $N$  time values,  $W_j$  is the time-dependent receiver-function error weighting,  $D_{\text{obs}}$  and  $D_{\text{syn}}$  are the Love and Rayleigh observed and synthetic phase-velocity curves with  $M$  values combined, and  $SW$  is the phase-velocity misfit cost weighting.

The only two adjustable parameters in the objective cost function are the weighting values of phase-velocity misfit and roughness. The relative weighting of the receiver function depends on a combination of the weighting of the dispersion and roughness. We find little difference between inversions with  $SW = 0.25$  and  $SW = 1.25$ , indicating little dependence on  $SW$ , so we choose  $SW = 1.0$  for all inversions described hereafter. We lower the roughness weighting for combined receiver-function phase-velocity inversions to  $RW = 0.0625$  from the receiver-function-only inversions that require  $RW = 0.25$ . This clearly demonstrates that including surface wave dispersion reduces the need for *a priori* smoothing constraints.

We choose to emphasize receiver function misfit for the 7 sec including and after the initial pulse by weighting the standard deviation as shown in Figure 2. We progressively down-weight each of the next 5 sec up to 25 sec. This encourages the NGA to preferentially model pulses that represent shallow structure. In addition, it de-emphasizes later multiples, which may not stack well even for bins with a narrow range of ray parameters.

The NGA chooses one elitist model per deme with the lowest objective cost to continue to the next generation without mutation, randomly mutating the model and recombining the model with other models associated with low cost. The first deme operates without the addition of an artificially high similarity cost. Models in the other three demes suffer similarity costs equal to the highest objective costs associated with any model in each deme. Similarity cost is only assigned to models with a difference metric less than a critical difference,  $R_C = 0.2$ , when compared with elitist models from higher-order demes (Koper *et al.*, 1999). Therefore, models in the second deme may suffer similarity costs only if they are similar to the elitist model from the first deme, whereas models of the third deme may suffer similarity costs because of similarity to the elitist models of the first and second deme. In this manner the NGA requires that the different demes search separate portions of the model space.

The demes must search unique portions of the model space, but the NGA does not necessarily require significant difference between the structures. For example, a given layer may alternatively be modeled as two layers of nearly similar velocity. By examining the elitist models, it is possible to determine how important a modeled structure is to fitting the observed data. Gradients, which are modeled with multiple layers, may not exhibit similar layer thickness or velocity while demonstrating similar profiles. Alternatively, if several models contain a significant interface at the same depth, the true structure likely contains an interface at that depth. The analysis of a suite of locally optimal models in addition

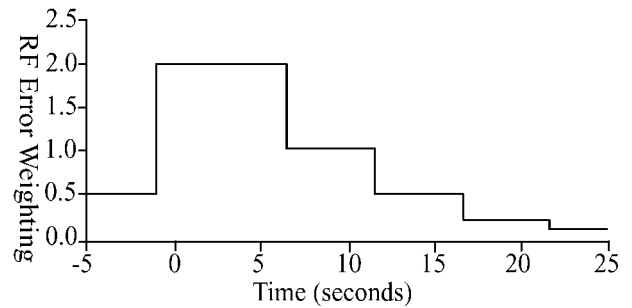


Figure 2. Receiver function error weighting as a function of time.

to analysis of a globally optimal model represents the compromise between linearized inversion techniques like Julia *et al.* (2000) and the neighborhood algorithms of Sambridge (1999a).

Smoothness constraints, although minimal, are critical in the inversion process. We choose the second derivative of velocity with respect to layer for reducing the frequency of modeled low-velocity zones without minimizing gradients. Because we do not desire to overlook strong interfaces or gradients with respect to depth, we calculate the roughness on a layer-by-layer basis, neglecting the layer thickness. Thus, a model may still find a large, sharp discontinuity by superposing several ultrathin layers without a prohibitive roughness cost.

Our structure models are only parameterized to a maximum of  $\sim 100$  km depth. For the purpose of computing synthetic dispersion curves we extend the structure to 400 km depth, with a velocity that linearly converges to IASP91 (Kennett and Engdahl, 1991). Therefore, phase velocities are extended to longer periods without requiring additional parameterization. Note that the peak sensitivity of the longest periods used here are about 150 km depth. Therefore, this parameterization has only minimal effect on the results while maintaining realistic models.

## Synthetic Tests

We demonstrate the effectiveness of the NGA receiver-function and phase-velocity technique by inverting a synthetic receiver function and synthetic Love and Rayleigh dispersion curves created from the nine-layer 1D model shown in Figure 3. This structure is also the globally optimal solution for the combined inversion of station MILO, thus allowing direct comparison between the synthetic test and inversion of the real data. The same test is repeated with and without noise contamination for multiple weighting schemes. Note that the synthetic receiver functions are calculated according to Ammon (1991), which is an acausal solution. Therefore, a small amount of receiver-function noise occurs prior to the initial  $P$  pulse. This noise is down-weighted in the receiver-function misfit weighting. When stacked, this random noise is reduced.

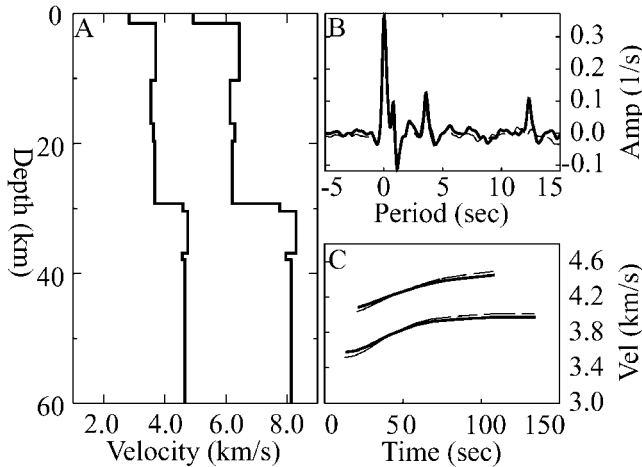


Figure 3. Synthetic “Test Structure” (A) with associated noiseless (solid line) and noisy (dashed line) receiver functions (B) and surface wave dispersion curves (C).

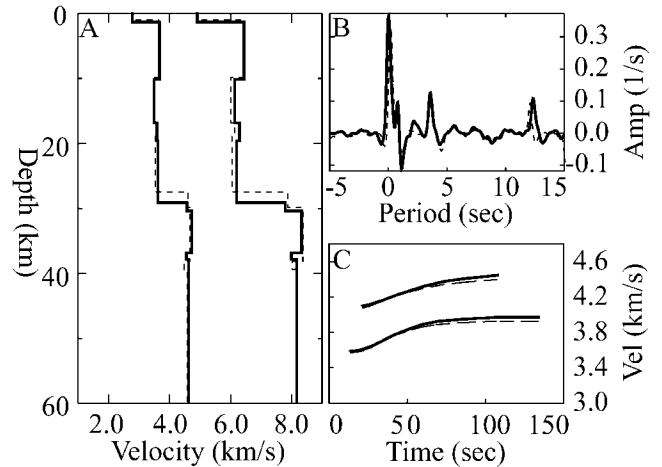


Figure 4. Noiseless synthetic (solid line) and NGA solution (dashed line) seismic structures (A) with associated receiver functions (B) and surface wave dispersion curves (C).

Use of the method described previously on the synthetic data results in a good match between the test model and the optimum model found by the NGA (Fig. 4). The method successfully locates interfaces of both the synthetic Moho and sediment–basement contact and even resolves two high-velocity layers in the crust. The standard deviation between test and optimal *P*- and *S*-wave velocities for all depths are less than 0.2 and 0.1 km/sec, respectively. Both interfaces of the Moho were located within 2 km of the test model. Several of the *P*-to-*S* converted multiples, which appear later on the receiver-function time series, are not well matched. This is caused by the receiver-function error weighting discussed above.

Noise is simulated by stacking eight receiver functions from multiple ray parameters with variable scatter and by adding two synthetic receiver functions of structures largely different from the synthetic receiver structure. Stacking receiver functions from multiple similar ray parameters is directly analogous to the stacking process we use for the observed data in Patagonia. Adding random contributions of dissimilar receiver functions to the synthetic receiver functions mimics a small degree of lateral heterogeneity and random noise. We also add twice the amount of noise to the dispersion curves as that found in Patagonia dispersion curves to emulate systematic problems associated with isolating phases on a phase-velocity curve that changes rapidly with period (Jenkins and Watts, 1968).

Adding noise to the receiver function reduces the signal of *P*-to-*S* converted multiples that arrive later in the test receiver function. The loss of these signals induces little change in results due to the error weighting of the receiver-function time series (Fig. 5). The systematic noise added to the test dispersion curve increases the gradient of the phase velocities for both Love and Rayleigh waves. Although the noise adversely affects the quality of the match between test

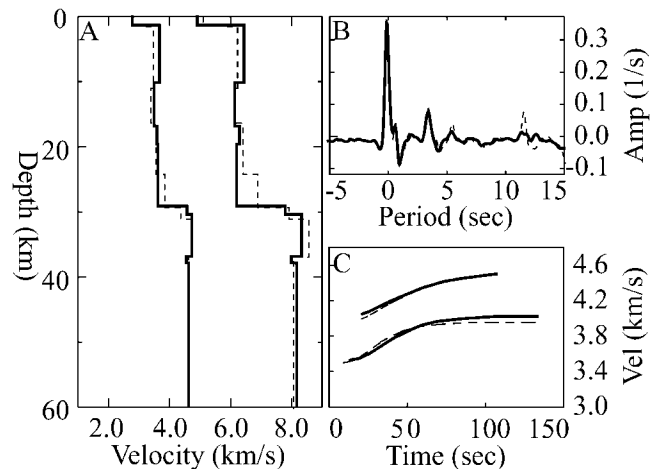


Figure 5. Noisy synthetic (solid line) and NGA solution (dashed line) seismic structures (A) with associated receiver functions (B) and surface wave dispersion curves (C).

and optimal models, the optimal structure is still quite similar. The *P*- and *S*-wave velocities for the entire model are within 0.3 and 0.2 km/sec of the test structure, respectively. The Moho and sediment–basement interfaces are located within 0.5 km of the test model. However, some of the smaller structures within the crust and mantle are more dissimilar. The average crustal *S* velocity is within 0.05 km/sec of the test structure.

The synthetic test demonstrates that the NGA receiver-function phase-velocity method can successfully model crustal and uppermost mantle structures with or without significant levels of noise. This technique can isolate crustal thickness, mean crustal velocity, sediment thickness, and

uppermost mantle velocity accurately without significant *a priori* constraints.

Some nonuniqueness still exists within the system. This may be seen in variation between locally optimal models. Although excellent agreement exists between the most optimal model and the test structure, other models are often either smoothed through the Moho region or possess very large low-velocity layers. Figure 6 demonstrates the structural match and variation between models. The most optimal model is a very close match to the test structure (low misfit cost). The second best (beta) model possesses a very smooth Moho and misses several of the finer structures. This deme achieves low cost by reducing the roughness cost. The third best (gamma) model, although very similar to the test structure, possesses a very smooth sub-Moho gradient and overlooks the sediment layer. Again this deme achieves low objective function cost by reducing the roughness cost. The delta deme locates a minimum that trades an excellent receiver function fit for a high model roughness cost due to a large low-velocity layer in the mantle.

There is no consistent trade-off between crustal thickness and crustal velocity as is common in receiver-function inversions. The model with the lowest phase-velocity misfit cost is also the most optimal model with the closest structure to the test structure. This indicates that including phase-velocity constraints in the receiver-function problem increases the uniqueness of the solution. Only models with proper velocities and, therefore, realistic interface depths may sufficiently model both the phase-velocity curve and receiver function. Other models minimize receiver-function misfit, phase-velocity misfit, or roughness rather than both receiver-function and phase-velocity misfit.

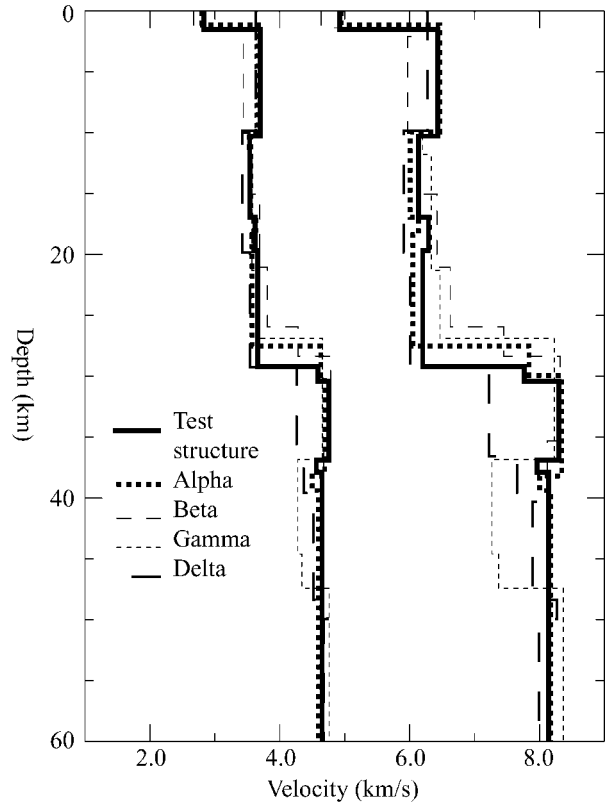


Figure 6. The synthetic test structure with the NGA globally and locally optimal structure solutions.

### Application: The Crustal Structure of Chilean Patagonia

#### Geological Setting of Patagonia

We apply the NGA receiver-function phase-velocity method to the crustal and upper mantle structure of Patagonia. Very little information exists on the deep structure of Patagonia, except for an onshore-offshore seismic refraction survey (Ludwig *et al.*, 1965). However, a small network of five broadband stations were operated there during 1997 and 1998 as part of the Seismic Experiment in Patagonia and Antarctica (Fig. 7) (Robertson *et al.*, 2003). This provides an opportunity to constrain the structure of this remote region using the NGA receiver-function phase-velocity method.

The tectonic history of southernmost South America may quickly be summarized by lower Paleozoic to lower Mesozoic accretionary prism formation (Dalziel and Brown, 1989), followed by extensional volcanism, resulting from the Late Jurassic Gondwana breakup and island arc collision with South America in the mid-Cretaceous forming the Andean Orogeny (Dalziel and Palmer, 1979). Denudation

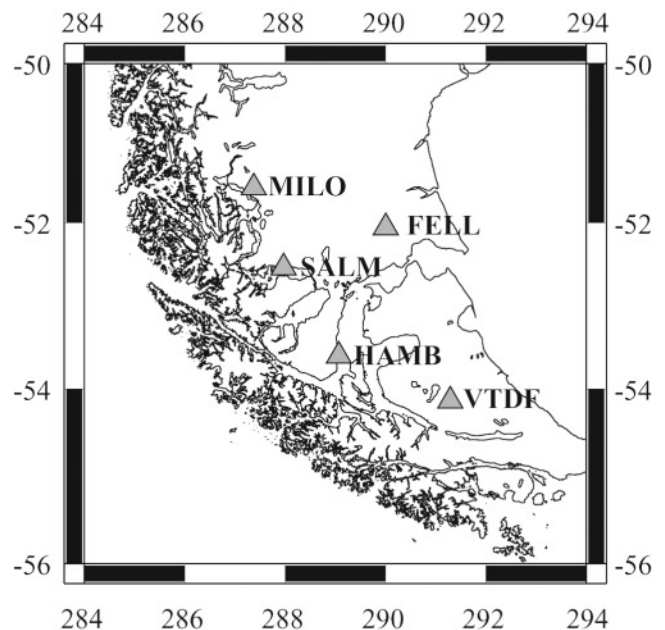


Figure 7. A map of the SEPA seismic stations used for application in Patagonia.

eroded the Austral Andes, infilling the Rocas Verdes basin with up to 6 km of volcanic arc sediments during the Late Jurassic-Early Cretaceous (Dalziel and Brown, 1989; Ludwig *et al.*, 1965). South America owes much of its more recent tectonics to Scotia plate-related motions. The Scotia plate relocated continental fragments over 1,000 km from Tierra del Fuego (Dalziel *et al.*, 1975). Late Cretaceous to present strike-slip faulting created the Patagonian Orocline (Pelayo and Wiens, 1989). Magnetism off the coast of Tierra del Fuego suggests 90° rotation along the oroclyne since the Late Jurassic, coinciding with Scotia motion (Cunningham *et al.*, 1991).

### Analysis

Rayleigh waves along nine distinct interstation paths from 18 events and Love waves along seven distinct interstation paths from 13 events were used for phase-velocity determination in Patagonia. Phase delays were measured using a phase-matched filter (Herrin and Goforth, 1977) prior to interstation modal isolation after Hwang and Mitchell (1986). The phase velocity is simply the interstation distance (difference between the radial event-to-station distances) divided by the interstation delay time. The dispersion curve for a given station is determined by averaging all interstation measurements containing that station. This produces some bias, because the paths are not centered beneath the station of interest; however, the region studied is rather small and is not expected to include substantial lateral variation. The Rayleigh wave standard deviation from mean phase velocity per period is  $\sim 0.035$  km/sec for short periods ( $T < 40$ ) and  $\sim 0.04$  km/sec for longer periods. The Love wave standard deviation from mean phase velocity per period is  $\sim 0.08$  km/sec and  $0.07$  km/sec for short and long periods. Figure 8 demonstrates the similarities and differences between the Patagonia phase-velocity curves.

We obtain about 20–30 receiver functions for each of the five Patagonia stations (Table 2) in the Seismic Experiment in Patagonia and Antarctica (SEPA) by using the iterative deconvolution technique (Ligorria and Ammon, 1999) on 35 events. Event selection criteria include magnitudes greater than 5.8 Mb, and epicentral distances between 30° and 90°. We stack radial receiver functions by 15° bins of epicentral distance to improve signal-to-noise ratios. For each station, more than 10 events are stacked with epicentral distances between 73° and 87°, and another 5 or more events with epicentral distances between 58 and 73. We use the 73–87° bin stacked receiver functions in this manuscript. Minimal radial or tangential receiver-function variation occurs as a result of azimuthal variation, suggesting the structure in this region is well modeled with horizontal interfaces. Note that later pulses, that are down-weighted in the time-dependent receiver function misfit weighting, do appear depending on azimuth, indicating deeper dipping interfaces at some stations. This is to be expected for stations near a shallow subduction zone.

We locate optimal 1D seismic models independently for

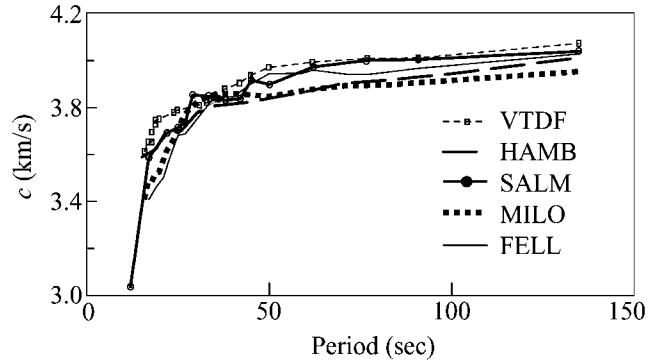


Figure 8. Rayleigh phase-velocity curves for each of the SEPA seismic stations.

Table 2  
Station List

Station	Latitude	Longitude	Station Location
MILO	−51.57	−72.62	Cueva del Milodon, Patagonia
FELL	−52.06	−70.00	Estancia Brazo Norte, Patagonia
SALM	−52.55	−72.03	Salmon Farm, Seno Skyring, Patagonia
HAMB	−53.61	−70.93	Puerto del Hambre, Patagonia
VTDF	−54.14	−68.71	Estancia Vicunna, Tierra del Fuego

The locations, latitude, and longitude of the SEPA seismic stations used in this study are shown.

each of the five SEPA stations. The *P*- and *S*-wave seismic profiles, phase velocities, and receiver functions are presented in Figure 9. Although presented here, the other locally optimal models located by the NGA often share similar sediment thickness, crustal thickness, and mean velocities to those observed with the globally optimal models. For example, the beta model for station SALM possesses the same Moho gradient as the optimal model but with different layer thickness and velocities for the smaller interfaces. This indicates that these interfaces are most likely less significant than the gradient they represent. In such models, we choose an interface depth corresponding to the largest stable velocity increase with a *P*-wave velocity of at least 7.7 km/sec. For SALM this is  $28 \pm 1$  km. While many of the globally optimal models possess low-velocity layers within the mantle, the depth and velocities of these layers are often not well resolved in other locally optimal models. This suggests that the location, and even presence of these layers, is nonunique. For this reason, we focus mainly on crustal thickness, sediment thickness, and mean velocities of the crust and mantle.

The mean crust and mantle *P*- and *S*-wave velocities and crustal thickness for each station are presented in Table 3. We also summarize corresponding results from Ludwig *et al.* (1965). Although the crustal seismic velocities are consistently low, they agree with Ludwig *et al.* (1965). By combining each of the 1D profiles, we create a sparsely sampled 3D seismic crustal and upper mantle model for Patagonia (Fig. 10). The region may be characterized by mean crust

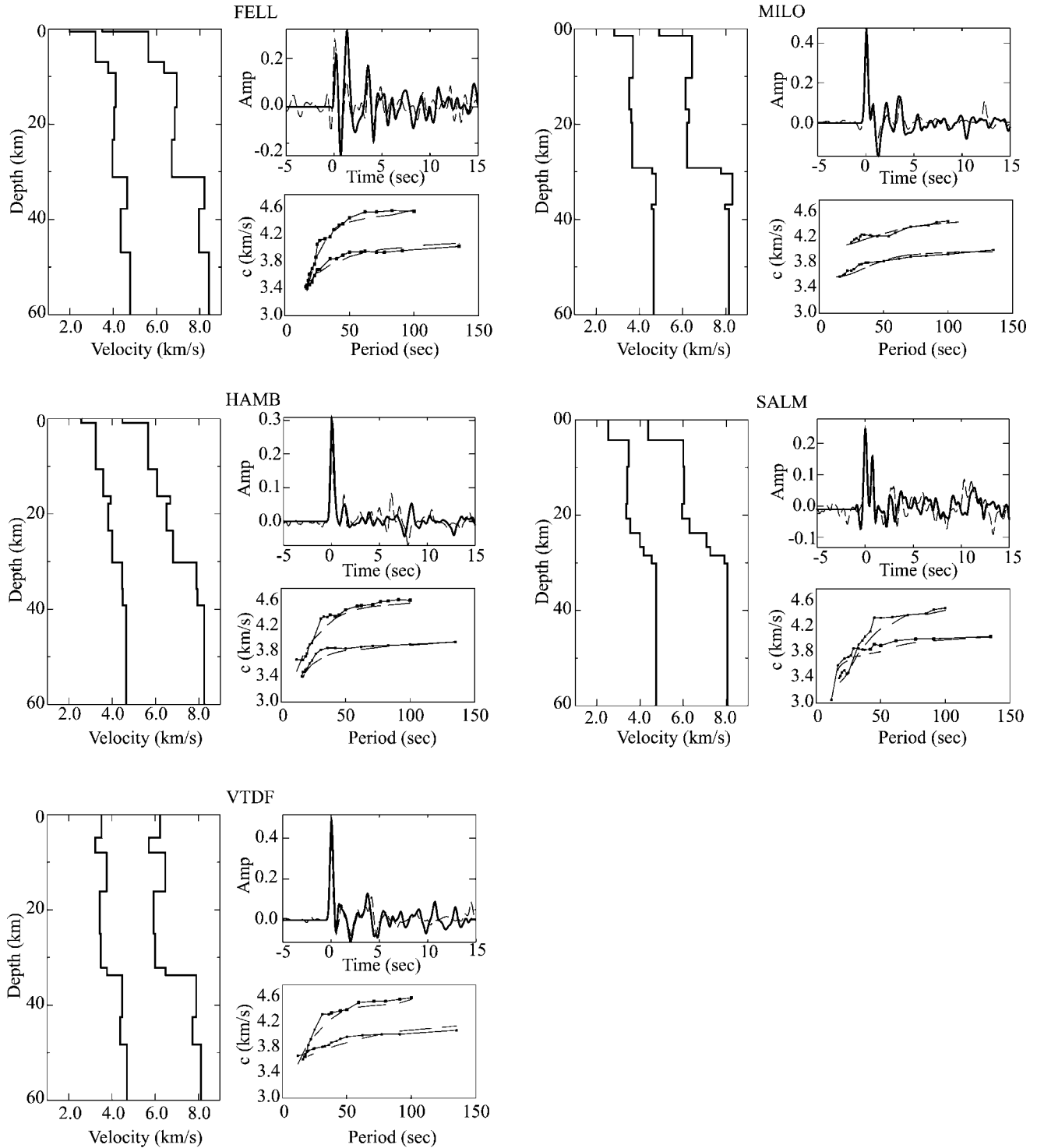


Figure 9. Observed (solid lines) and NGA solutions (dashed lines) to seismic structure, receiver functions, and phase-velocity curves for the Patagonia seismic stations.

and mantle shear velocities of  $3.55 \pm 0.12 \text{ km/sec}^{-1}$  and  $4.71 \pm 0.18 \text{ km/sec}^{-1}$ , and mean crustal thickness of  $30.7 \pm 1.8 \text{ km}$ . Removing sediment layers results in a mean shear crustal basement velocity of  $3.65 \pm 0.10 \text{ km/sec}^{-1}$ . Modeled sediment thickness increases and Moho depth decreases

toward station SALM, in agreement with the results from Ludwig *et al.* (1965). It is unlikely that the observed relationship between sediment and crustal thickness is due to inversion trade-off between velocity and Moho depth because the receiver functions and phase velocities are well fit,

Table 3  
Summary of Patagonia Models

Station	Layer Thickness			Crustal Velocities			Mantle Velocities	
	$H_c$	$H_s$		$V_{\beta c}$	$V_{ac}$	$V_{am}$	$V_{\beta m}$	
FELL	31.1	0.6	2	3.74	6.40	8.44	4.78	
MILO	30.4	1.5		3.62	6.23	8.14	4.65	
SALM	28.1	29.6	5	3.33	5.86	8.11	4.79	
HAMB	30.2	0.9	1	3.56	6.11	8.25	4.65	
VTDF	33.7	34.7	0	3.52	6.10	8.11	4.68	
Average	30.7	1.5		3.55	6.14	8.21	4.71	
$\sigma^2$	1.8	1.5		0.13	0.18	0.13	0.06	
$\% \sigma^2 / ave$	5.89	100		3.82	2.91	1.53	1.36	

Displayed are: the sediment ( $H_s$ ) and crust thickness ( $H_c$ ) and  $P$ - and  $S$ -wave velocities of the crust ( $V_{ac}$  and  $V_{\beta c}$ ) and uppermost mantle ( $V_{am}$  and  $V_{\beta m}$ ) for each station. Equivalent results close to the stations from Ludwig *et al.* (1965) are presented in italics. We note the level of variation from Patagonia average values with standard deviation ( $\sigma^2$ ) and standard deviation as a percentage of the average value for Patagonia ( $\% \sigma^2 / ave$ ).

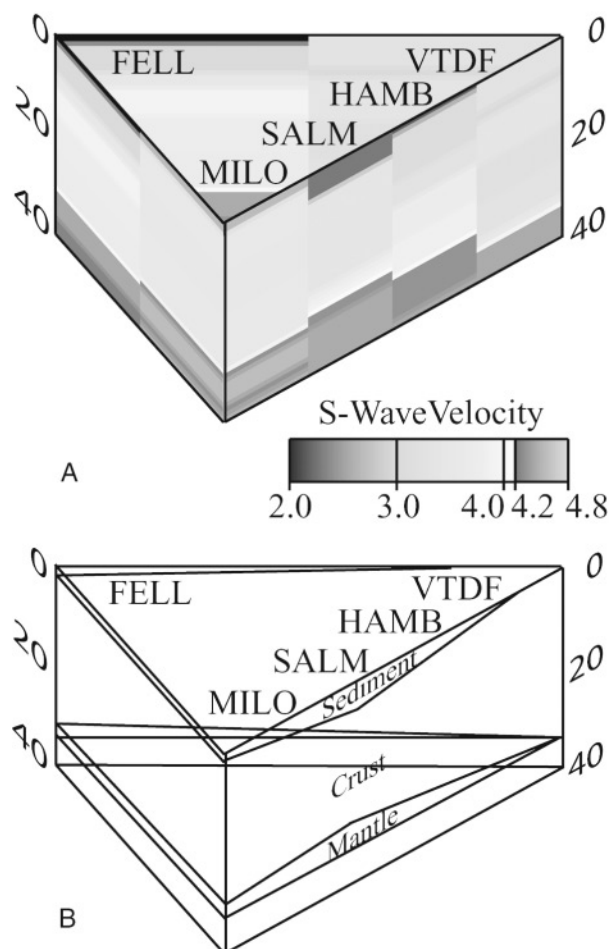


Figure 10. (A) 3D compilation of the 1D seismic profiles shown in Figure 8. (B) Interpretation.

and there is little evidence of a velocity-depth trade-off in the results from the other niches of the NGA inversion.

These results are consistent with the limiting assumptions that all layers are horizontal and isotropic. Although there is topography to the Moho and sediment layers, the dip of these layers is negligible. Both Rayleigh and Love wave phase velocities are matched for all stations, suggesting there is insufficient anisotropy in the region to adversely affect this study. Although Robertson *et al.* (2003) found ~5% polarization anisotropy in the upper mantle, the path lengths of that study extended far to the north, beyond the area analyzed here. Apparently such large upper mantle anisotropy does not extend immediately beneath the SEPA Patagonia array.

Interpretation

Results from the combined receiver function-phase velocity NGA analysis technique show that Patagonia is characterized by a well resolved Moho ranging from 28 to 34 km depth. This compares favorably with the previous seismic refraction results of 30–35 km depth (Ludwig *et al.*, 1965), and with the results of regional waveform inversion (26–36 km), which provide an average over a much larger region (Robertson *et al.*, 2003). Also, the NGA analysis discloses a lower-velocity sediment layer of variable thickness (0–4.3 km thick), also in general agreement with previous results.

In addition to being consistent with refraction results, the models presented previously are consistent with the geological history of Patagonia. Figure 10 illustrates the vertically exaggerated geometry of Patagonia sediment, basement, and mantle. The thickness of the sediment layer is inversely proportional to the total crustal thickness. This is particularly true for station SALM, which shows the thickest sediment layer (4.3 km) and the thinnest total crustal thickness (28 km). The coincident sediment thickening and crustal thinning beneath station SALM is consistent with

geological models for the the denudation of the Austral Andes and infilling of the Rocas Verdes basin (Dalziel and Brown, 1989; Ludwig *et al.*, 1965), which formed as a result of crustal thinning during Jurassic extension.

The presented models suggest that the sediment layer of the Rocas Verde basement probably formed through isostatic subsidence because of crustal thinning from  $\sim 34$  km to  $\sim 24$  km as a result of extensional tectonics. The Rocas Verdes basin formed as a result of sediment influx into the basin from the Austral Andes denudation, which thickened the current crust underlying the Rocas Verdes by  $\sim 4$  km to its current thickness of  $\sim 28$  km. Regions to the north and south of station SALM, which experienced less thinning and influx, possess thicker crustal structures with thinner layers of sediment.

The current variations in sediment and crustal thickness seem to be largely load balanced. Using standard conversions for density from compressional velocity, we calculate sediment, crust, and mantle densities for each model (Ammon, 1991; Kennett, 1983). The resultant sediment loads and mantle loads down to 34 km are, respectively, 96% and 99.9%, inversely correlated with basement loads down to the Moho. The net result is that sediment and mantle loads balance more than 98% of the 17% crustal load variation. Within the resolution of the NGA receiver-function phase-velocity inversion technique, Patagonia sediment and crustal thickness are currently load balanced.

### Conclusions

The NGA, when applied to the combined receiver-function and phase-velocity inversion problem, results in accurate and unique solutions. We demonstrate the accuracy of the technique with a synthetic test. Tests with and without noise show that velocities and layer depths are well constrained, as well as overall structure. Moho depths and sediment layer thickness are particularly well resolved. Application of this method to real data from the SEPA Patagonia array yields coherent 1D models for each station. When these 1D models are examined collectively, they provide a sparse 3D model, which is consistent with previous active source experiments and reflects Patagonia's tectonic history.

The NGA receiver-function and phase-velocity method works well with little *a priori* knowledge of the structure. This technique does not require layer thickness, starting models, or even a large number of layers to produce a unique solution. This analysis method is ideal for regions such as Patagonia, where few previous comprehensive studies constrain seismic structure. By solving for layer thickness in addition to seismic velocity, we reduce the necessity for many thin (0.5–2 km thick) layers. The NGA can model gradients, sharp contrasts, and low-velocity layers by simply thinning, contrasting, and inverting velocities for layers. As a result, resolution of sharp boundaries, such as sediment-basement and the Moho, may be increased. The depth pa-

rameterization allows the NGA to focus on depths that relate to unique phases in each observed receiver-function and phase-velocity curve.

The NGA also demonstrates the importance of particular features for modeling receiver functions and phase-velocity curves by producing locally optimal models in addition to the globally optimal model. By comparing the locally optimal models, it is possible to determine which features are most important to modeling the receiver function and examine the solution space for obvious trade-offs. By analyzing the suite of optimal models rather than only the lowest-cost solution, it is possible to gain better insight into the uniqueness of the result and the robustness of individual features.

Applying this method to data from a deployment of five broadband stations in Chilean Patagonia yields a regional model of crustal structure and thickness that is consistent with the geological history of the region. Sediment thickness is inversely proportional to crustal thickness, with sediment thicknesses of more than 4 km in the western portions where the crustal thickness is a relatively thin 28 km. This is consistent with previous geological studies, which suggest that the Rocas Verdes basin in western Patagonia formed by crustal thinning, isostatic compensation, and subsequent sedimentation.

### Acknowledgments

We thank Keith Koper for assistance with NGA inversion code and Bob Herrmann for assistance with surface wave dispersion measurements and modeling. We also thank Rodrigo Adaros, Sergio Barrientos, George Helffrich, Stacey Robertson Maurice, Patrick Shore, and Emilio Vera for collecting the Patagonia broadband data. Suzan van der Lee and an anonymous reviewer are thanked for their thorough and insightful comments and suggestions. This research was conducted with support from National Science Foundation Grants OPP9527366 and OPP9814622.

### References

- Aki, K., and P. G. Richards (1980). *Quantitative Seismology: Theory and Methods*, W. H. Freeman, New York.
- Ammon, C. J. (1991). The isolation of receiver effects from teleseismic *P* waveforms, *Bull. Seism. Soc. Am.* **81**, 2504–2510.
- Ammon, C. J., G. E. Randall, and G. Zandt (1990). On the non-uniqueness of receiver function inversions, *J. Geophys. Res.* **95**, 15,303–15,318.
- Burdick, L. J., and C. A. Langston (1977). Modeling crustal structure through the use of converted phases in teleseismic body-wave forms, *Bull. Seism. Soc. Am.* **67**, 677–691.
- Cassidy, J. F. (1995). A comparison of the receiver structure beneath stations of the Canadian National Seismograph Network, *Can. J. Earth Sci.* **32**, 938–951.
- Clayton, R. W., and R. A. Wiggins (1976). Source shape estimation and deconvolution of teleseismic body waves, *Geophys. J. R. Astron. Soc.* **47**, 151–177.
- Clitheroe, G., O. Gudmundsson, and B. L. N. Kennett (2000). Sedimentary and upper crustal structure of Australia from receiver functions, *Aust. J. Earth Sci.* **47**, 209–216.
- Cunningham, D. W., K. A. Klepeis, W. A. Gose, and I. W. E. Dalziel (1991). The Patagonian Orocline: New paleomagnetic data from the Andean magmatic arc in Tierra Del Fuego, Chile, *J. Geophys. Res.* **196**, 16,061–16,069.

- Dalziel, I. W. D., and R. L. Brown (1989). Tectonic denudation of the Darwin metamorphic core complex in the Andes of Tierra Del Fuego, southern most Chile: implications for cordilleran orogenesis, *Geology* **17**, 699–703.
- Dalziel, I. W. D., and K. F. Palmer (1979). Progressive deformation and orogenic uplift at the southern extremity of the Andes, *Geol. Soc. Am. Bull.* **90**, 259–280.
- Dalziel, I. W. D., R. H. Dott, J. R. D. Winn, and R. L. Bruhn (1975). Tectonic relations of South Georgia to the southernmost Andes, *Geol. Soc. Am. Bull.* **86**, 1034–1040.
- Du, Z. J., and G. R. Foulger (1999). The crustal structure beneath the north-west fjords, Iceland, from receiver functions and surface waves, *Geophys. J. Int.* **139**, 419–432.
- Dueker, K. G., and A. F. Sheehan (1997). Mantle discontinuity structure from mid-point stacks of converted P to S waves across the Yellowstone Hotspot Track, *J. Geophys. Res.* **102**, 8313–8327.
- Goldberg, D. E. (1989). *Genetic Algorithms in Search, Optimization, and Machine Learning*, Addison-Wesley, Reading, Massachusetts.
- Gurrola, H., G. E. Baker, and J. B. Minster (1995). Simultaneous time-domain deconvolution with application to the computer of receiver functions, *Geophys. J. Int.* **120**, 537–543.
- Herrin, E., and T. Goforth (1977). Phase-matched filters: application to the study of Rayleigh Waves, *Bull. Seism. Soc. Am.* **67**, 1259–1275.
- Herrmann, R. B. (1978). *Computer Programs in Earthquake Seismology*, Vol. 2, *Surface Wave Programs*, Department of Earth and Atmospheric Sciences, Saint Louis University, St. Louis, Missouri.
- Hwang, H. J., and B. J. Mitchell (1986). Interstation surface wave analysis by frequency domain Wiener deconvolution and modal isolation, *Bull. Seism. Soc. Am.* **76**, 847–864.
- Jenkins, G., and D. Watts (1968). *Spectral Analysis and Its Applications*, Holden-Day, San Francisco.
- Julia, J., C. J. Ammon, R. B. Herrmann, and A. M. Correig (2000). Joint inversion of receiver function and surface wave dispersion observations, *Geophys. J. Int.* **143**, 99–112.
- Kennett, B. L. N. (1983). *Seismic Wave Propagation in Stratified Media*, Cambridge University Press, New York.
- Kennett, B. L. N., and E. R. Engdahl (1991). Traveltimes for global earthquake location and phase identification, *Geophys. J. Int.* **105**, 429–465.
- Koper, D. K., M. E. Wyssession, and D. A. Wiens (1999). Multimodal function optimization with a niching genetic algorithm: a seismological example, *Bull. Seism. Soc. Am.* **89**, 978–988.
- Langston, C. A. (1979). Structure under Mount Rainier, Washington, inferred from teleseismic body waves, *J. Geophys. Res.* **83**, 4749–4762.
- Last, R. J., A. A. Nyblade, C. A. Langston, and T. J. Owens (1997). Crustal structure of the East African Plateau from receiver functions and Rayleigh wave phase velocities, *J. Geophys. Res.* **102**, 24,469–24,483.
- Ligorria, J. P., and C. J. Ammon (1999). Iterative deconvolution and receiver-function estimation, *Bull. Seism. Soc. Am.* **89**, 1395–1400.
- Ludwig, W. J., J. I. Ewing, and M. Ewing (1965). Seismic-refraction measurements in the Magellan Straits, *J. Geophys. Res.* **70**, 1855–1876.
- Mafoud, S. W. (1995). Niching methods for genetic algorithms, *Ph.D. Thesis*, University of Illinois at Urbana-Champaign.
- Menke, W. (1984). *Geophysical Data Analysis: Discrete Inverse Theory*, Academic Press, New York.
- Owens, T. J., G. Zandt, and S. R. Taylor (1984). Seismic evidence of an ancient rift beneath the Cumberland Plateau, Tennessee: a detailed analysis of broadband teleseismic P waveforms, *J. Geophys. Res.* **89**, 7783–7795.
- Ozalaybey, S., M. K. Savage, A. F. Sheehan, J. N. Louie, and J. N. Brune (1997). Shear-wave velocity structure in north basin and range province from the combined analysis of receiver functions and surface waves, *Bull. Seism. Soc. Am.* **87**, 183–189.
- Park, J., and V. Levin (2000). Receiver functions from multiple-taper spectral correlation estimates, *Bull. Seism. Soc. Am.* **90**, 1507–1520.
- Pelayo, A. M., and D. A. Wiens (1989). Seismotectonics and relative plate motion in the Scotia Sea region, *J. Geophys. Res.* **94**, 7293–7320.
- Randall, G. E. (1989). Efficient calculation of differential seismograms for lithospheric receiver functions, *Geophys. J. Int.* **99**, 469–481.
- Robertson, M. S., D. A. Wiens, K. D. Koper, and E. Vera (2003). Crustal and upper mantle structure of southernmost South America inferred from regional waveform inversion, *J. Geophys. Res.* **108** (B1), 2038.
- Sambridge, M. (1999a). Geophysical inversion with a neighbourhood algorithm. I. Searching a parameter space, *Geophys. J. Int.* **138**, 479–494.
- Sambridge, M. (1999b). Geophysical inversion with a neighbourhood algorithm. II. Appraising the ensemble, *Geophys. J. Int.* **138**, 727–746.
- Sheehan, A., G. Abers, C. Jones, and A. Lerner-Lam (1995). Crustal thickness variations across the Colorado Rocky Mountains from teleseismic receiver functions, *J. Geophys. Res.* **100**, 20,391–20,404.
- Shibutani, T., M. Sambridge, and B. Kennett (1996). Genetic algorithm inversion for receiver functions with application to crust and uppermost mantle structure beneath East Australia, *Geophys. Res. Lett.* **23**, 1829–1832.
- Takeuchi, H., and M. Saito (1972). Seismic surface waves, *Methods Comput. Phys.* **11**, 217–302.
- Wiens, D. A. (1998). Seismic experiment in Patagonia and Antarctica (SEPA), *IRIS Newsletter* **17**, 9–11.

Department of Earth and Planetary Science  
Washington University  
St. Louis, Missouri

Manuscript received 15 August 2003.